Dynamics Analysis and Control of a Large wingspan Flapping-Wing Vehicle

Chenguang Zhai[1], Bifeng Song[1,2], Qiang Fu[1,2,*], Jianlin Xuan[1,2], Junying Li[1]

[1]Northwestern Polytechnical University, Xi' an 710072, China
[2]National Key Laboratory of Aircraft Configuration Design, Xi' an 710072, China

Abstract

In this paper, we investigate the dynamics modeling and control approaches for a large wingspan flapping-wing vehicle (LWFWV). To balance modeling accuracy and efficiency, we adopt separate modeling approaches for the aerodynamic components: the flapping wings and the tail assembly. The aerodynamic model for the flapping wings is derived from wind tunnel experiments, while the tail assembly's model, similar to that of fixed-wing vehicles, is established using empirical estimation methods. The equations of motion for the vehicle are obtained using the single rigid-body method. We employ periodic averaging theory to linearize the model, resulting in a linear time-invariant system. The system's stability is assessed based on the eigenvalue distribution of the transfer function matrix. Subsequently, we design the attitude controller based on the cascade PID algorithm and the position controller based on the total energy control algorithm. The effectiveness of the controllers is verified through numerical simulations and flight experiments.

Keywords: Large wingspan flapping-wing vehicle; Wind tunnel experiment; Attitude control; Position control

1. Introduction

The bird-like flapping-wing vehicle is an unmanned aerial vehicle that emulates the flight mechanisms of birds [1]. These vehicles primarily operate in level flight, with flapping frequencies ranging from 3 to 20 Hz. The flapping plane is generally perpendicular to the flight direction, generating lift and thrust primarily through the down stroke of the wings, while attitude control is achieved via the tail. Current research predominantly focuses on insect-like flapping-wing vehicles or micro bird-like flapping-wing vehicles [2]-[5], with relatively limited studies on large wingspan flapping-wing vehicles (LWFWVs). LWFWVs offer significant advantages such as enhanced camouflage, extended endurance, low noise, and the ability to carry larger payloads, presenting extensive application prospects. To accelerate the practical development of LWFWVs, this paper investigates their dynamics and control systems.

The dynamic system of flapping-wing vehicles comprises both aerodynamic models and equations of motion. Due to the periodic aerodynamic forces generated by the flapping wings, this system is typically a time-varying nonlinear system, which complicates modeling and analysis. Several mainstream methods are currently available to address this issue. Regarding aerodynamic models, computational fluid dynamics (CFD) methods based on the Navier-Stokes equations are widely used. These methods provide high computational accuracy and are suitable for studying the effects of motion parameters and geometric parameters on the aerodynamic characteristics of the vehicle. However, CFD methods are time-consuming and computationally expensive, making them unsuitable for the rapid modeling required in dynamic studies. As a result, some researchers have turned to empirical estimation methods [6]-[9]. Enhancements to strip theory have been made by incorporating vortex-wake effects, partial leading-edge suction, and post-stall characteristics, resulting in a modified unsteady aerodynamic model. This model is further simplified using first-order or higher-order

averaging theories, facilitating a better understanding of the flight stability and dynamic characteristics of flapping-wing vehicles. This approach has been widely applied in the modeling and control studies of flapping-wing vehicles. Other researchers have adapted fixed-wing aerodynamic modeling methods[10]-[11]. They obtain aerodynamic data near the flight state points through wind tunnel experiments to build a database. Interpolation tables are then used to derive the aerodynamic model for flapping-wing vehicles. This model is linearized using periodic averaging methods, yielding high-accuracy models in a shorter time and allowing for rapid analysis of the vehicle's dynamic characteristics.

Regarding the equations of motion, both single rigid-body and multi-body methods are employed in the dynamic modeling of flapping-wing vehicles[12]-[15]. The single rigid-body method is commonly used, treating the vehicle as a single rigid body and employing Newton-Euler equations to establish the dynamics model. This approach is relatively simple. The multi-body method considers the vehicle as comprising multiple rigid bodies, such as the fuselage, flapping wings, and tail. Analytical mechanics are used to establish the dynamics model, making this approach relatively complex. The choice of method depends on the specific modeling requirements. Based on the aforementioned research advancements, it is now feasible to establish a dynamic model for large wingspan flapping-wing vehicles (LWFWVs) with reasonable accuracy, suitable for dynamic analysis and control.

The control problem of flapping-wing vehicles requires solutions tailored to the characteristics of the dynamic system. Ephrahim et al. utilized a quasi-steady aerodynamic model coupled with the single rigid-body motion equation to develop a periodic flight dynamics model for bird-like flapping-wing vehicles [16]. They represented the trimmed flight state using a limit cycle and assessed the stability of this limit cycle by estimating the system's eigenvalues through averaging methods. Based on this model, they designed and compared the performance of a proportional-derivative (PD) controller, a discrete-time linear-quadratic regulator (LQR) controller, and a discrete-time periodic linear quadratic Gaussian (LQG) controller. He et al. developed a single rigid-body dynamics model for bird-like flapping-wing vehicles with flat wings using quasi-steady aerodynamic theory and Newton-Euler equations [17]. Through dynamic analysis, they determined that the system is uncontrollable at all static equilibrium points. To address this, they proposed a closed-loop feedback controller based on dynamic compensation to stabilize the system along a dynamic trajectory. The effectiveness of this controller was validated through prototype experiments. Balaji et al. constructed an aerodynamic model for bird-like flapping-wing vehicles using a modified strip theory, integrating it with the multi-body motion equation that consider the flapping wing's shape to propose a general model [18]. They developed a model reference adaptive controller (MRAC) to achieve stable flight and used error metrics to evaluate the control performance. They compared the MRAC’s performance with that of an adaptive bias controller with a PI component, and an adaptive bias controller with a PD component.

In this paper, we investigate the dynamics modeling and control approaches for the LWFWV. To balance modeling accuracy and efficiency, we adopt a separate modeling approach for the aerodynamic components: the flapping wings and the tail assembly. The aerodynamic model for the flapping wings is derived from wind tunnel experiments. Given the similarity of the LWFWV's tail assembly to that of fixed-wing vehicles, its aerodynamic model is established using empirical estimation methods. The equations of motion for the vehicle are obtained using the single rigid-body method. We employ periodic averaging theory to linearize the model, resulting in a linear time-invariant system. The system's stability is assessed based on the eigenvalue distribution of the transfer function matrix. Subsequently, we design the longitudinal attitude and position control systems.

This paper is organized as follows. In Section II, we present the dynamics of the LWFWV based on wind tunnel experiments and empirical estimation methods. Section III details the design of the LWFWV control system. In Section IV, we report the experimental results of the flight control of the LWFWV prototype. Finally, Section V provides a summary and conclusions.

2. System Model

2.1 System Definition

The robotic vehicle used in this study is a motor-driven LWFWV, a brid-like prototype developed by our research team. Figure 1 illustrates the structure and major components, including the flapping wings with their corresponding mechanisms, the tail assembly, avionics, and the battery. The wings possess a single degree of freedom (DoF) for flapping, while rotation around the leading edge during flapping occurs passively, generating both primary thrust and lift for flight. The tail assembly comprises the horizontal stabilizer and the vertical stabilizer. Symmetrical deflection of the horizontal stabilizer control surface induces a pitch moment, while differential deflection of the tail surfaces generates a roll moment.

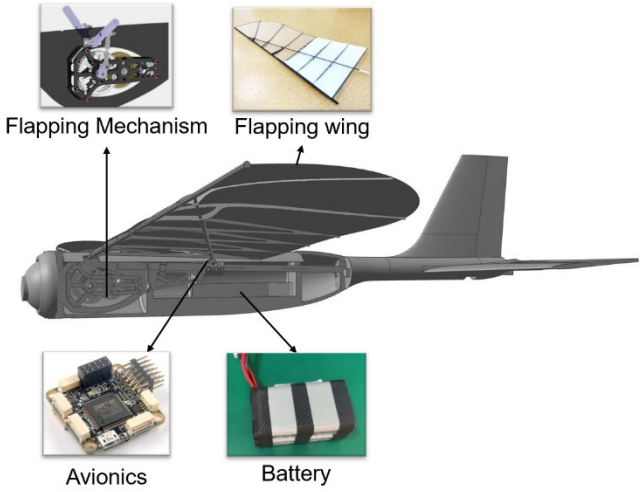

Figure 1 – The CAD structure demonstration of LWFWV.

2.2 Aerodynamic Modeling of the LWFWV

There are several methods for aerodynamic modeling of a bird-like flapping wing vehicle, including empirical estimation, Computational Fluid Dynamics (CFD), and wind tunnel experiment. The empirical estimation method relies on existing empirical formulas to simplify the modeling process. However, current research predominantly focuses on insect-like flapping wing micro vehicles and fixed-wing vehicles, leading to reduced accuracy for bird-like models. The CFD method offers high flexibility and low cost but is typically time-consuming, making it unsuitable for initial design, evaluation and dynamic simulation of bird-like flapping wing vehicles. The wind tunnel experiment can measure the aerodynamic characteristics of flapping wings in various states using experimental balances. This method provides high measurement accuracy and good repeatability. However, when conducting whole-vehicle wind tunnel experiments, the number of experimental factors increases, adding to the model's complexity.

To improve modeling efficiency while ensuring accuracy, this paper adopts a separate modeling approach for the aerodynamic models of the flapping wings and the tail assembly. The aerodynamic model of the flapping wings is established using the wind tunnel experiment. Since the tail assembly of the LWFWV is similar to that of fixed-wing vehicle, its aerodynamic model is established using the empirical estimation method.

2.2.1 Aerodynamic Modeling of the Flapping Wings

The complete experimental setup for the measurement of aerodynamic forces and moments is shown in Figure 2. A six-axis sensor(ME K6D40) with a measurement range of ±200 N and ±10 Nm is placed at the wing root to measure the forces and moments. A global filter is used to denoise the experimental data.

During the experiment, the flapping amplitude of the wings is fixed at the same value as during actual flight. The wind speed, flapping frequency, and angle of attack are selected as experimental factors, as shown in Table 1.

Table 1 The ranges of the experimental parameters for the wind tunnel experiment.

Experimental Parameters	Value
Wind speed (m/s)	6.5, 7.5, 8.5, 9.5, 10.5
Flapping frequency (Hz)	2, 3, 4
Angle of attack (deg)	0, 5, 10, 15
Flapping amplitude (deg)	45

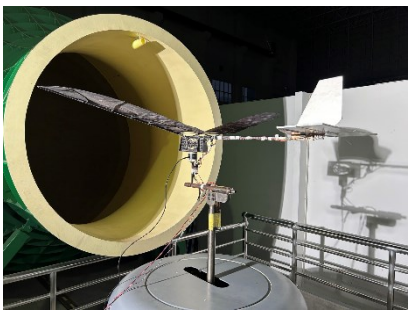

Figure 2 – Measurement of wing forces and moments.

The instantaneous aerodynamic forces and moments of the flapping wings obtained through wind tunnel experiments exhibit strong nonlinearity. The purpose of establishing the aerodynamic model of the flapping wings in this paper is to serve as input for the flight dynamics model of the vehicle. Therefore, periodic averaging will be applied to the instantaneous aerodynamic forces and moments to simplify the model.

According to the post-processing results of the wind tunnel experimental data for the flapping wings, the period-averaged lift is linearly related to the angle of attack before stall, and this phenomenon remains consistent regardless of variations in wind speed and flapping frequency.

As shown in Figure 3, variations in wind speed at a constant flapping frequency and variations in flapping frequency at a constant wind speed do not affect the linear relationship between the angle of attack and the period-averaged lift.

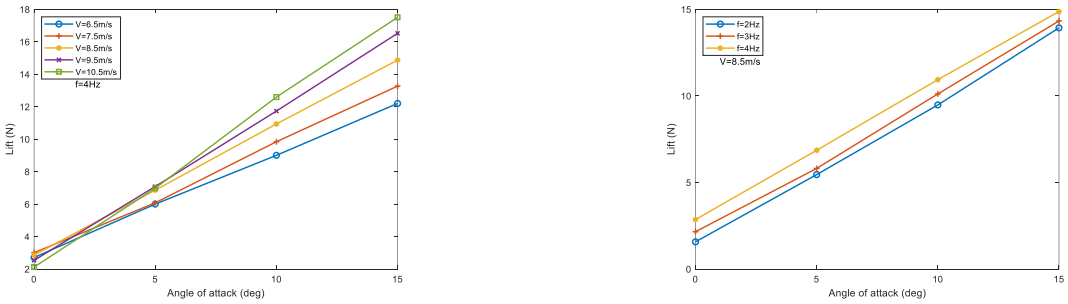

Figure 3 – The relationship between period-averaged lift and angle of attack for the flapping wings.

Therefore, the period-averaged lift model for the flapping wing can be expressed as *Equation 1*, where the slope of the period-averaged lift line $\bar{L}_\alpha$ and the period-averaged lift at zero angle of attack $\bar{L}_0$ are both independent of the angle of attack.

$$\bar{L} = \bar{L}_\alpha \alpha + \bar{L}_0 \tag{1}$$

When modeling the slope of the period-averaged lift line and the period-averaged lift at zero angle of attack, overfitting and abrupt changes outside the experimental range should be avoided. Therefore, a polynomial model is used, as shown in *Equation 2*.

$$\begin{cases} \bar{L}_\alpha = -0.06645 + 0.1063V - 0.0057f \\ \bar{L}_0 = -1.275 + 0.6424V + 0.4108f - 0.056V^2 + 0.02725Vf \end{cases} \tag{2}$$

The thrust characteristics of the flapping wing are similar to those of a propeller, with the period-averaged thrust being proportional to the square of the flapping frequency. This overall trend remains consistent across different angles of attack and wind speeds, as demonstrated by the wind tunnel experimental results shown in Figure 4.

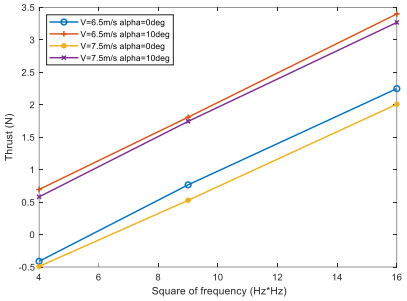

Figure 4 – Period-averaged thrust is linearly related to the square of the flapping frequency.

The period-average thrust model can be expressed as *Equation 3*, where the thrust coefficient $\bar{T}_f$ and the steady-state drag D are both independent of the flapping frequency.

$$\bar{T} = \bar{T}_f f^2 + D \tag{3}$$

Coefficients are fitted using a polynomial model, as shown in *Equation 4*.

$$\begin{cases} \bar{T}_f = 0.3544 - 0.02235V - 0.004389\alpha + 0.0003911V^2 + 0.0006938V\alpha \\ D = -3.346 + 0.7162V - 0.1321\alpha - 0.05934V^2 + 0.01739V\alpha - 0.01079\alpha^2 \end{cases} \tag{4}$$

According to the wind tunnel experimental results, the average pitching moment is linearly related to the angle of attack, and this linear relationship is not affected by flapping frequency or wind speed, as shown in Figure 5.

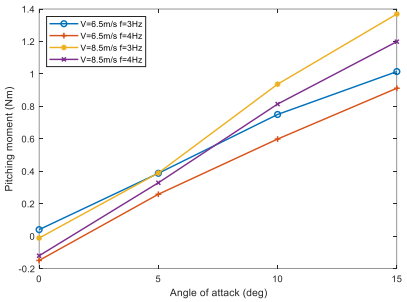

Figure 5 – Period-averaged pitching moment is linearly related to the angle of attack.

The period-average pitching moment model can be expressed as *Equation 5*, where $\bar{M}_\alpha$ is the slope of the period-averaged pitching moment line and $\bar{M}_0$ is the period-averaged pitching moment at zero angle of attack.

$$\bar{M} = \bar{M}_\alpha \alpha + \bar{M}_0 \tag{5}$$

Coefficients are fitted using a polynomial model, as shown in *Equation 6*.

$$\begin{cases} \bar{M}_\alpha = -0.001388 + 0.0118V - 0.002074f \\ \bar{M}_0 = 0.7315 - 0.08248V - 0.1043f + 0.01621Vf - 0.01904f^2 \end{cases} \tag{6}$$

2.2.2 Aerodynamic Modeling of the Tail Assembly

In the empirical estimation method, dimensionless force coefficients and moment coefficients are generally used to represent aerodynamic forces and moments, as shown in *Equation 7*, where ρ is the air density, S is the reference area of the tail, and c is the mean aerodynamic chord length of the tail. Z_L and X_D are the components of the aerodynamic force in the wind coordinate frame, corresponding to the lift coefficient C_L and drag coefficient C_D, respectively. M is the component of the aerodynamic moment in the body-fixed frame, corresponding to the moment coefficient C_m.

$$\begin{cases} [X_D, Z_L]^{\mathrm{T}} = \dfrac{1}{2}\rho \mathrm{V}^2 \mathrm{S}[\mathrm{C_D}, \mathrm{C_L}]^{\mathrm{T}} \\ \mathrm{M_t} = \dfrac{1}{2}\rho \mathrm{V}^2 \mathrm{ScC_m} \end{cases} \tag{7}$$

The aerodynamic force and moment coefficients can be expressed as a summation of various aerodynamic derivatives based on empirical formulas, as shown in *Equation 8*. The aerodynamic derivatives are calculated using the vortex lattice method, as shown in Table 2.

$$\begin{cases} C_L = C_{L0} + C_{L\alpha}\alpha + C_{L\delta_e}\delta_e \\ C_D = C_{D0} + kC_L^2 \\ C_m = C_{m0} + C_{m\alpha}\alpha + C_{mq}\dfrac{c}{2V}q + C_{m\delta_e}\delta_e \end{cases} \tag{8}$$

Table 2 The estimation results of aerodynamic derivative

Aerodynamic Derivative	C_{L0}	$C_{L\alpha}$	$C_{L\delta_e}$	C_{D0}	k	C_{m0}	$C_{m\alpha}$	C_{mq}	$C_{m\delta_e}$
Value	0	0.054	0.043	0.019	0.115	0.002	-0.108	-5.033	-0.096

2.3 Body Dynamic Modeling of the LWFWV

In this subsection, the body dynamic model is derived using the Newton-Euler Equations for a single rigid body, as listed below:

$$\begin{cases} m\dfrac{d\boldsymbol{V}^b}{dt} = \boldsymbol{F}^b - m\boldsymbol{\omega}^b \times \boldsymbol{V}^b \\ \boldsymbol{J}\dfrac{d\boldsymbol{\omega}^b}{dt} = \boldsymbol{M}^b - \boldsymbol{\omega}^b \times \boldsymbol{J}\boldsymbol{\omega}^b \end{cases} \tag{9}$$

where $\boldsymbol{V}^b = [u \quad v \quad w]^{\mathrm{T}}$ is the velocity vector of the CG of the LWFWV system in the body-fixed frame, $\boldsymbol{\omega}^b = [p \quad q \quad r]^{\mathrm{T}}$ is the angular velocity vector of the CG of the LWFWV system in the body-fixed frame, m is the total mass of the LWFWV system. $\boldsymbol{J}$ is the moment of inertia of the LWFWV body relative to the body-fixed frame, and we assume that $\boldsymbol{J}$ is a constant matrix. $\boldsymbol{F}^b$ and $\boldsymbol{M}^b$ are the total forces and moments of the LWFWV system in the body-fixed frame, as shown in *Equation 10*, where $\boldsymbol{F}_w$ and $\boldsymbol{F}_t$ represent the aerodynamic forces of the flapping wing and the tail, respectively. $\boldsymbol{M}_w$ and $\boldsymbol{M}_t$ represent the aerodynamic moments of the flapping wing and the tail, respectively. $\boldsymbol{G}$ represents the gravitational force. R_{bw} is the rotation matrix from the wind coordinate frame to the body-fixed frame, and R_{be} is the rotation matrix from the inertial frame to the body-fixed frame.

$$\begin{cases} \boldsymbol{F}^b = \boldsymbol{F}_w + R_{bw}\boldsymbol{F}_t + R_{be}\boldsymbol{G} \\ \boldsymbol{M}^b = \boldsymbol{M}_w + \boldsymbol{M}_t \end{cases} \tag{10}$$

$$R_{bw}=\begin{bmatrix}\cos\alpha\cos\beta & -\sin\beta\cos\alpha & -\sin\alpha\\ \sin\beta & \cos\beta & 0\\ \sin\alpha\cos\beta & -\sin\beta\sin\alpha & \cos\alpha\end{bmatrix} \tag{11}$$

$$R_{be}=\begin{bmatrix}\cos\psi\cos\theta & \sin\psi\cos\theta & -\sin\theta\\ \cos\psi\sin\theta\sin\phi-\sin\psi\cos\phi & \sin\psi\sin\theta\sin\phi+\cos\psi\cos\phi & \cos\theta\sin\phi\\ \cos\psi\sin\theta\cos\phi+\sin\psi\sin\phi & \sin\psi\sin\theta\cos\phi-\cos\psi\sin\phi & \cos\theta\cos\phi\end{bmatrix} \tag{12}$$

2.4 Model linearization and analysis

The model established above is nonlinear and challenging to analyze. To simplify the complex dynamic model and highlight its major properties, the steady straight and level flight condition is chosen as the equilibrium point, and the nonlinear equations are linearized using the Taylor formula. The final linearized model is shown in *Equation 13*.

$$\dot{\boldsymbol{X}}=A\boldsymbol{X}+B\boldsymbol{U} \tag{13}$$

Where

$$\boldsymbol{X}=[V\quad \alpha\quad q\quad \theta]^{T} \tag{14}$$

$$\boldsymbol{U}=[\delta_e\quad \delta_f]^{\mathrm{T}} \tag{15}$$

$$A=\begin{bmatrix}X_V & X_\alpha & X_q & X_\theta\\ Z_V & Z_\alpha & Z_q & Z_\theta\\ M_V & M_\alpha & M_q & M_\theta\\ 0 & 0 & 1 & 0\end{bmatrix} \tag{16}$$

$$B=\begin{bmatrix}X_{\delta_e} & X_{\delta_f}\\ Z_{\delta_e} & Z_{\delta_f}\\ M_{\delta_e} & 0\\ 0 & 0\end{bmatrix} \tag{17}$$

Applying the Laplace transformation to *Equation 13* under the condition $\boldsymbol{X}(0)=0$, the transfer function matrix is obtained, as shown in *Equation 18*.

$$G(s)=(sI-A)^{-1}B \tag{18}$$

The eigenvalues of the transfer function matrix are shown in *Equation 19.*

$$\lambda_{1,2}=-0.0728\pm 0.4083i,\ \lambda_3=-2.9393,\ \lambda_4=-0.0398 \tag{19}$$

λ_1 and λ_2 are a pair of complex conjugate roots, both with negative real parts, representing a convergent oscillatory mode. λ_3 and λ_4 are both negative real numbers, representing monotonic convergent modes. Based on the above analysis, the LWFWV exhibits longitudinal dynamic stability. A step signal is applied to the system, and the open-loop response of the pitch rate and pitch angle is analyzed using numerical simulation methods. The results are shown in Figure 6. When the pitch rate is subjected to a unit step disturbance, it oscillates for approximately 7 seconds before converging to 0.4. As the pitch rate remains non-zero, the pitch angle will continuously increase. Therefore, designing a closed-loop control system is essential to achieve pitch angle tracking control and alleviate the operational burden on the vehicle.

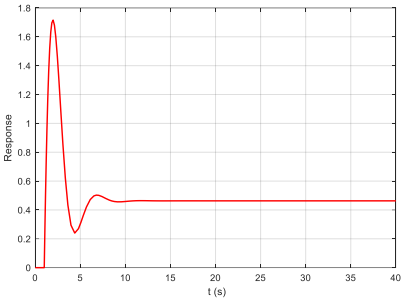

(a) The unit step response results for the pitch rate

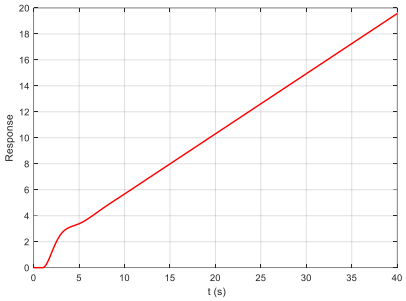

(b) The unit step response results for the pitch

Figure 6 – The unit step response results for the pitch rate and pitch angle.

3. Control of the LWFWV

3.1 Longitudinal Attitude Control System Design

To maintain the current pitch angle flight of the LWFWV when there is no pitch control command, and to maintain and track the pitch angle corresponding to the command when there is a pitch control command, we have designed the longitudinal attitude control system. The system is designed based on a cascaded PID algorithm [19], achieving stable control of the pitch rate loop and the pitch angle loop, the control structure diagram is shown in Figure 7.

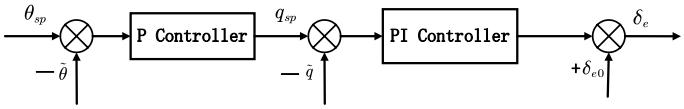

Figure 7 – The Longitudinal pitch control system block diagram.

The transfer function from the elevator to the pitch rate is shown in *Equation 20*, which is used as the mathematical model for the pitch rate loop.

$$\frac{q}{\delta_e} = \frac{-3.9013s^3 - 0.8907s^2}{s^4 + 3.1246s^3 + 0.7226s^2 + 0.5294s + 0.0201} \tag{20}$$

The servo model in the loop can be simplified to a first-order inertial element, with the time constant obtained from the datasheet, as shown in *Equation 21*.

$$G_a = -\frac{1}{0.124s + 1} \tag{21}$$

A PI controller is designed for the pitch rate loop, and its unit step response is shown in Figure 8. As depicted, the controller demonstrates a good response.

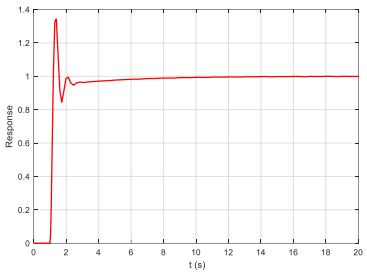

Figure 8 – Step response results of pitch Angle velocity control system.

The relationship between the pitch rate and the pitch angle of the LWFWV during steady straight and level flight is given in *Equation 22*. Therefore, the pitch angle control loop can be established based on the pitch rate control loop.

$$\Delta\theta = s\Delta q \tag{22}$$

Adding a P controller to this loop yields good control performance, as shown in the unit step response in Figure 9. The settling time of the system is approximately 5.9 seconds, with no overshoot.

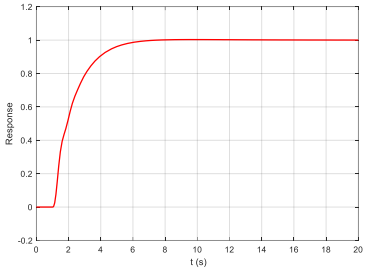

Figure 9 – Step response results of pitch Angle control system.

Based on the simulation results above, the longitudinal attitude control system design is completed.

3.2 Longitudinal Position Control System Design

To track and maintain the speed and altitude of the LWFWV, a longitudinal position control system was designed. By applying the total energy control system (TECS) algorithm, the system controls the flapping frequency to achieve the required total energy for flight and adjusts the pitch angle to distribute kinetic and potential energy [20]. This approach effectively decouples the control of speed and altitude.

The TECS algorithm takes the speed setpoint V_{sp} and altitude setpoint h_{sp} as inputs and combines them with the corresponding state feedback signals. Through the control law algorithm, the pitch angle setpoint θ_{sp} and flapping frequency setpoint f_{sp} are obtained. The pitch angle setpoint θ_{sp} is input into the inner loop longitudinal attitude control system, while the flapping frequency setpoint f_{sp} directly affects the LWFWV, achieving simultaneous control of speed and altitude.

The total energy of the LWFWV is shown in *Equation 23*, where E_T is the total energy of the LWFWV, m is the total mass of the LWFWV, V is the airspeed of the LWFWV, h is the flight altitude of the LWFWV, and g is the gravitational acceleration.

$$E_T = \frac{1}{2}mV^2 + mgh \tag{23}$$

Differentiating the total energy with respect to time and performing nondimensionalization yields the rate of energy change, as shown in *Equation 24*, where γ represents the flight path angle of the LWFWV.

$$\dot{E} = \frac{\dot{V}}{g} + \frac{\dot{h}}{V} = \frac{\dot{V}}{g} + \sin(\gamma) \tag{24}$$

The force balance equation of the LWFWV in the thrust direction is shown in *Equation 25*.

$$T = mg\left(\frac{\dot{V}}{g} + \sin(\gamma)\right) \approx mg\left(\frac{\dot{V}}{g} + \gamma\right) \tag{25}$$

From this, it can be observed that the rate of energy change of the aircraft is linearly related to the net thrust. Therefore, the total energy of the aircraft can be controlled by controlling the net thrust. For LWFWV, the flapping frequency has the greatest impact on the net thrust, hence controlling the flapping frequency can achieve control over the total energy.

After achieving total energy control through flapping frequency, it is necessary to distribute the kinetic and potential energy to achieve simultaneous control of speed and altitude. Kinetic and potential energy distribution is accomplished using pitch angle. The energy difference, defined as potential energy minus kinetic energy, is expressed in *Equation 26*.

$$B = mgh - \frac{1}{2}mV^2 \tag{26}$$

Differentiating it with respect to time and performing nondimensionalization yields the energy balance rate, as shown in *Equation 27*.

$$\dot{B} = \frac{\dot{h}}{V} - \frac{\dot{V}}{g} \tag{27}$$

Summarizing the above control principles, the system block diagram is shown in Figure 10.

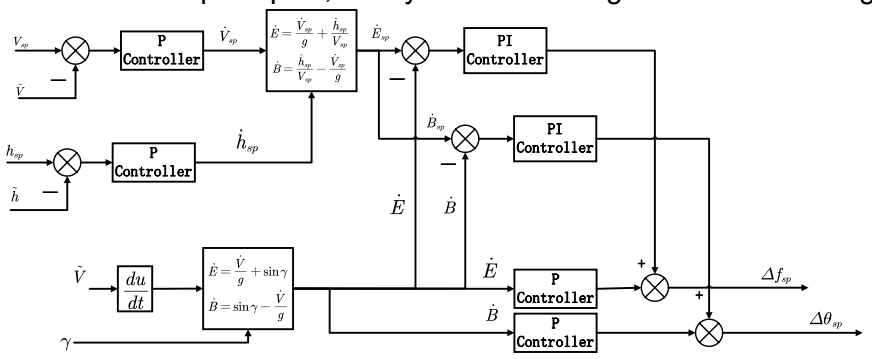

Figure 10 – The TECS algorithm control block diagram.

Proportional control is used to obtain the desired rate of speed change and the desired rate of climb, as shown in *Equation 28*.

$$\begin{cases} \dot{V}_{sp} = K_V \left(V_{sp} - V \right) \\ \dot{h}_{sp} = K_h \left(h_{sp} - h \right) \end{cases} \tag{28}$$

Using PI control, the energy change rate and energy balance rate are respectively mapped to the flapping frequency and pitch angle. To avoid introducing unnecessary zeros, the proportional term uses the actual values instead of the deviation values, yielding the desired changes in flapping frequency and pitch angle, as shown in *Equation 29*.

$$\begin{cases} \Delta f_{sp} = K_P^E \dot{E} + K_i^E \int \left(\dot{E}_{sp} - \dot{E} \right) dt \\ \Delta \theta_{sp} = K_P^B \dot{B} + K_i^B \int \left(\dot{B}_{sp} - \dot{B} \right) dt \end{cases} \tag{29}$$

To perform a simulation analysis of the longitudinal position control system, initial conditions are set with an altitude of 30m and a speed of 8.5m/s. The target values are set to 40m and 10m/s, respectively, and applied to the system as step inputs. The system response is shown in Figure 11.

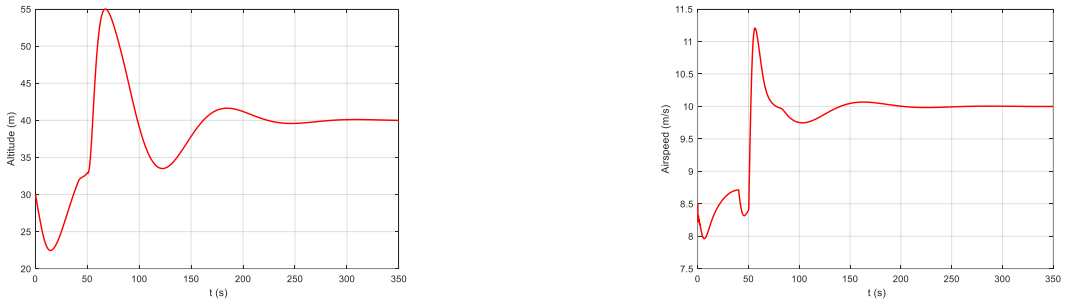

(a) Step response results of altitude (b) Step response results of airspeed

Figure 11 – Step response results of longitudinal position control system.

From the figure, it can be observed that both altitude and speed exhibit significant overshoot during the initial response. However, both parameters converge to their setpoints around 200 seconds. This indicates that the longitudinal position control system effectively manages the control of flight altitude and speed.

4. Prototype Experiments

The modeling approach and the closed-loop controller presented in the previous sections have been

verified by an LWFWV prototype as shown in Figure 12. Its main parameters are listed in Table 3.

Figure 12 – Flight experiment of the LWFWV prototype.

Table 3 Main parameters of LWFWV.

Parameters	Attributes
Mass	1.147kg
Span	1.8m
Span-chord Ratio	6.4
Cruising Speed	8.5m/s
Servos	12g micro digital servos
Flight Controller	Pixracer r15
Motor	2312 brushless motor
Battery	6200mAh 4S lithium polymer battery

The LWFWV employs a hand-launched takeoff assisted by a manual run-up. During the flight, the longitudinal attitude controller operates continuously. The displacement of the longitudinal pitch channel stick on the remote control corresponds to the pitch angle setpoint of the LWFWV, while the throttle channel stick directly controls the throttle value of the LWFWV.

Figure 13 illustrates the performance of the longitudinal attitude controller in regulating the pitch angle. The red line represents the pitch angle setpoint, while the black line shows the real-time pitch angle. Throughout the flight, the trend in the aircraft's pitch angle closely follows the setpoint. The periodic oscillations in the actual pitch angle likely result from the forces exerted on the central body by the flapping wings. Overall, the longitudinal attitude controller demonstrates good time-domain tracking performance.

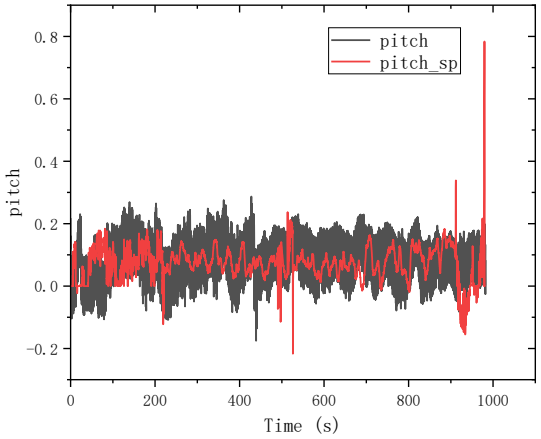

Figure 13 – Actual control effect of longitudinal pitch Angle control system.

Once the LWFWV transitions from takeoff to level flight, the longitudinal position controller is employed to maintain constant altitude and speed. The displacement of the throttle stick on the

remote control corresponds to the speed setpoint, with zero displacement indicating cruise speed. Similarly, the displacement of the pitch stick controls the flight altitude, and zero displacement results in maintaining the current altitude.

Figure 14 shows the controller's performance in regulating the airspeed of the LWFWV. The black line represents the actual airspeed, while the red line indicates the controller's airspeed setpoint. During the period from 0 to 50 seconds, the throttle stick displacement on the remote control is small, resulting in a lower airspeed setpoint and causing the actual airspeed to be higher than the setpoint. However, the actual airspeed tracks the setpoint. From 50 to 300 seconds, the actual airspeed closely follows the setpoint, which varies based on the throttle stick displacement. Between 300 and 700 seconds, the airspeed setpoint is fixed at 8.5 m/s, with the actual airspeed consistently oscillating around the setpoint.

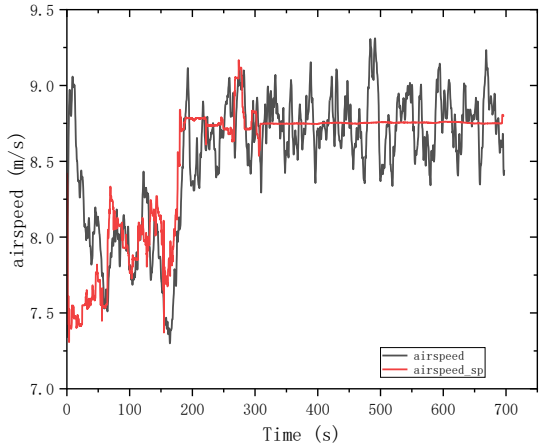

Figure 14 – Actual airspeed control effect of longitudinal position control system.

Figure 15 shows the controller's performance in regulating the altitude of the LWFWV. From 0 to 300 seconds, the pitch stick on the remote control remains in a neutral position, resulting in an altitude setpoint of 65 meters. The actual altitude hovers around this setpoint. Between 300 and 700 seconds, the altitude setpoint is adjusted to 70 meters, and the actual altitude consistently remains close to the setpoint. Overall, the longitudinal position controller demonstrates good tracking performance.

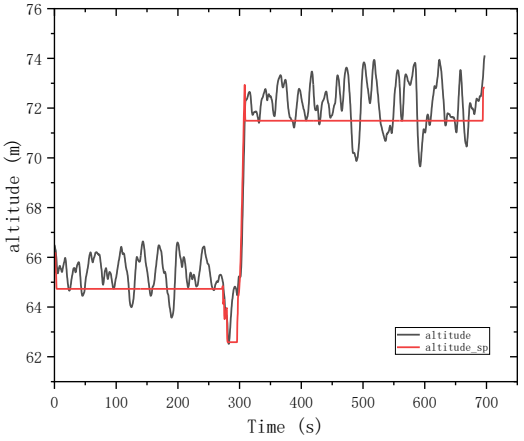

Figure 15 – Actual altitude control effect of longitudinal position control system.

5. Conclusion

On the basis of the wind tunnel experiment and the empirical estimation method, the dynamics model of a LWFWV is presented in this paper. By qualitatively analyzing the properties of the dynamics model, it is shown that the system has dynamic stability in the constant speed level flight state. To enhance the stable flight capability of the LWFWV, a longitudinal attitude control system and a longitudinal position control system are designed. The effectiveness of these control systems is

validated through numerical simulations and flight experiments. Based on the above work, the analysis of the lateral dynamic system of the LWFWV and the design of the corresponding control system will be the focus of future work.

6. Contact Author Email Address

mailto: foxfu@nwpu.edu.cn

7. Copyright Statement

The authors confirm that they, and/or their company or organization, hold copyright on all of the original material included in this paper. The authors also confirm that they have obtained permission, from the copyright holder of any third party material included in this paper, to publish it as part of their paper. The authors confirm that they give permission, or have obtained permission from the copyright holder of this paper, for the publication and distribution of this paper as part of the ICAS proceedings or as individual off-prints from the proceedings.

8. References

[1] Mackenzie, D. A Flapping of Wings[J]. Science, 2012,335(6075):1430-1433.
[2] Keennon M, Grasmeyer J. Development of two MAVs and vision of the future of MAV design[C]//AIAA International Air and Space Symposium and Exposition: The Next 100 Years. 2003: 2901.
[3] Chen A, Song B, Wang Z, et al. A Novel Actuation Strategy for an Agile Bioinspired FWAV Performing a Morphing-Coupled Wingbeat Pattern[J]. IEEE Transactions on Robotics, 2022.
[4] Xuan J, Song B, Yang W, et al. Progress of Chinese “Dove” and future studies on flight mechanism of birds and application system[J]. Transactions of Nanjing University of Aeronautics & Astronautics, 2020, 37(5): 663-675.
[5] Siqi W, Bifeng S, Ang C, et al. Modeling and flapping vibration suppression of a novel tailless flapping wing micro air vehicle[J]. Chinese Journal of Aeronautics, 2022, 35(3): 309-328.
[6] DeLaurier J D. An aerodynamic model for flapping-wing flight[J]. The Aeronautical Journal, 1993, 97(964): 125-130.
[7] Lee Y J, Lua K B, Lim T T, et al. A quasi-steady aerodynamic model for flapping flight with improved adaptability[J]. Bioinspiration & biomimetics, 2016, 11(3): 036005.
[8] Harmon R, Grauer J, Hubbard J, et al. Experimental determination of ornithopter membrane wing shapes used for simple aerodynamic modeling[C]//26th AIAA Applied Aerodynamics Conference. 2008: 6237.
[9] Han J S, Chang J W, Han J H. An aerodynamic model for insect flapping wings in forward flight[J]. Bioinspiration & biomimetics, 2017, 12(3): 036004.
[10] Nian P, Song B, Xuan J, et al. A wind tunnel experimental study on the flexible flapping wing with an attached airfoil to the root[J]. IEEE access, 2019, 7: 47891-47903.
[11] Nian P, Song B, Xuan J, et al. Study on flexible flapping wings with three dimensional asymmetric passive deformation in a flapping cycle[J]. Aerospace Science and Technology, 2020, 104: 105944.
[12] Doman D B, Oppenheimer M W, Sigthorsson D O. Wingbeat shape modulation for flapping-wing micro-air-vehicle control during hover[J]. Journal of guidance, control, and dynamics, 2010, 33(3): 724-739.
[13] Dickinson M H, Lehmann F O, Sane S P. Wing rotation and the aerodynamic basis of insect flight[J]. science, 1999, 284(5422): 1954-1960.
[14] Bolender M. Rigid multi-body equations-of-motion for flapping wing mavs using kane's equations[C]//AIAA Guidance, Navigation, and Control Conference. 2009: 6158.
[15] Khosravi M, Novinzadeh A B. A multi-body control approach for flapping wing micro aerial vehicles[J]. Aerospace Science and Technology, 2021, 112: 106525.
[16] Dietl J M, Garcia E. Stability in ornithopter longitudinal flight dynamics[J]. Journal of Guidance, Control, and Dynamics, 2008, 31(4): 1157-1163.
[17] He G, Su T, Jia T, et al. Dynamics analysis and control of a bird scale underactuated flapping-wing vehicle[J]. IEEE Transactions on Control Systems Technology, 2019, 28(4): 1233-1242.
[18] Chandrasekaran B K, Steck J E. An adaptive flight control system for a flapping wing aircraft[C]//2018 AIAA Guidance, Navigation, and Control Conference. 2018: 1836.
[19] Bennett S. Development of the PID controller[J]. IEEE Control Systems Magazine, 1993, 13(6): 58-62.
[20] Faleiro L F, Lambregts A A. Analysis and tuning of a ‘Total Energy Control System’control law using eigenstructure assignment[J]. Aerospace science and technology, 1999, 3(3): 127-140.